Deep learning approaches for intraoperative pixel-based diagnosis of colon cancer metastasis in a liver from phase-contrast images of unstained specimens

Sitnik, Dario, Aralica, Gorana, Pačić, Arijana, Popović Hadžija, Marijana, Hadžija, Mirko, et al.

Dario Sitnik, Gorana Aralica, Arijana Pačić, Marijana Popović Hadžija, Mirko Hadžija, Ivica Kopriva, "Deep learning approaches for intraoperative pixel-based diagnosis of colon cancer metastasis in a liver from phase-contrast images of unstained specimens," Proc. SPIE 11320, Medical Imaging 2020: Digital Pathology, 1132009 (16 March 2020); doi: 10.1117/12.2542799

SPIE.

Event: SPIE Medical Imaging, 2020, Houston, Texas, United States

Deep Learning Approaches for Intraoperative Pixel-based Diagnosis of Colon Cancer Metastasis in a Liver from Phase-contrast Images of Unstained Specimens

Dario Sitnik[1], Gorana Aralica[2, 3] , Arijana Paćić[2], Marijana Popović Hadžija[4], Mirko Hadžija[4], and Ivica Kopriva[1*]

[1]Division of Electronics, Ruđer Bošković Institute, Bijenička cesta 54, P.O. Box 180, 10002, Zagreb, Croatia
[2]Department of Pathology and Cytology, Clinical Hospital Dubrava, Avenija Gojka Šuška 6, 10000 Zagreb, Croatia
[3]School of Medicine, University of Zagreb, Šalata 3, 10000 Zagreb, Croatia
[4]Division of Molecular Medicine, Ruđer Bošković Institute, Bijenička cesta 54, 10000 Zagreb, Croatia

e-mail: Dario.Sitnik@irb.hr, garalica@kbd.hr, arijanapacic@yahoo.com, Marijana.Popovic.Hadzija@irb.hr, Mirko.Hadzija@irb.hr, ikopriva@irb.hr

Abstract

There is a need for computer-aided diagnosis (CAD) systems to relieve the workload on pathologists. This seems to be especially important for intraoperative diagnosis during surgery, for which diagnostic time is very limited. This paper presents preliminary results of intraoperative pixel-based CAD of colon cancer metastasis in a liver from phase-contrast images of unstained frozen sections. In particular, two deep learning networks: the U-net and the structured autoencoder for deep subspace clustering, were trained on eighteen phase-contrast images belonging to five patients and tested on eight images belonging to three patients. Spectrum angle mapper was also used in comparative performance analysis. The best result achieved by the U-net yielded balanced accuracy of 83.70%±8%, sensitivity of 94.50%±8%, specificity of 72.9%±8% and Dice coefficient of 45.20%±25.4%. However, factors such as absence of tissue fixation and ethanol-induced dehydration, melting of the specimen under the microscope and/or frozen crystals in the specimen cause variations in quality of phase-contrast images of unstained frozen sections. This, in return, affects reproducibility of diagnostic performance.

Keywords: U-net, Structured autoencoders, intraoperative diagnosis, colon cancer metastasis in a liver, phase-contrast imaging, unstained specimens.

1. INTRODUCTION

According to the International Agency for Research on Cancer of the World Health Organization, there were 14 million new cases and 8 millions of cancer-related deaths in 2012 [1]. 10% of diagnosed cases among men and 9.2% among women relates to colorectal cancer. Although

Medical Imaging 2020: Digital Pathology, edited by John E. Tomaszewski, Aaron D. Ward, Proc. of SPIE Vol. 11320, 1132009 · © 2020 SPIE
CCC code: 1605-7422/20/$21 · doi: 10.1117/12.2542799

imaging for cancer screening has been investigated for a long time [2], biopsy is the only method for confident diagnosis of cancer. Collected tissue samples are fixed across a glass slide for subsequent microscopic examination. Diagnosis is set by pathologist through visual inspection of histopathological samples. That represents a gold standard for diagnosis of almost all types of cancers [3], [4]. However, due to the raise in cancer incidence, diagnoses and grading of cancer is becoming increasingly complex and highly time-consuming task for pathologists [4], [5], [6]. Hence, there is a need for computer-aided diagnoses (CAD) to relieve the workload on pathologists [4]-[9]. To improve visibility of tissue structures, histopathological samples are dyed with one or more stains. The stain used by pathologists for over a hundred years is hematoxylin-eosin (H&E). Hematoxylin stains cell nuclei blue, while eosin stains cytoplasm and connective tissue pink. Fixation is ensured through formalin-fixed paraffin-embedding (FFPE) and that, typically, takes 48 hours to prepare. However, for intraoperative diagnosis during surgery, which is of interest in this paper, diagnostic time is very limited and rapid frozen section is used instead of FFPE section [8]. That, however, influences tissue morphology and, consequently, quality of staining, which even in a case of FFPE is burdened with experimental variations known as batch effects [10]. Hence, hard constraint imposed on diagnostic time during surgery in combination with staining associated batch effects stand for motivation to validate possibility of CAD diagnosis using phase-contrast images of the frozen sections of unstained histopathological specimens. As pointed in [8], very few researches have analyzed frozen sections so far [11], [12]. The most important reason is that number of slides samples for analysis is insufficient. That creates major problem for machine learning-based CAD systems even when specimens are stained, in particular for convolutional neural networks (CNNs)-based deep learning (DL) structures, which require large amount of annotated (labeled) training data [9], [7], [5], [13], [14], [15]. Above statement is even truer for the images of unstained frozen sections. This paper presents preliminary results for pixel-based diagnosis of the colon cancer metastasis in a liver using phase-contrast images of unstained frozen sections. In particular, the structured autoencoder (SAE) for deep subspace clustering [16] and the pre-trained U-net [17], were trained and validated on phase-contrast images of eighteen sections collected from five patients, and tested on eight phase-contrast images collected from three patients. Furthermore, spectrum angle mapper (SAM) classifier has also been used for diagnosis. To the best of our knowledge this is the first work attempting to discriminate metastatic colon cancer cells in liver from non-cancerous cells in intraoperative diagnosis using images of unstained frozen sections. The rest of the paper is organized as follows. Section 2 presents materials and methods used for this research. Section 3 presents conducted experiments and obtained results. Section 4 discusses obtained results. Section 5 presents conclusions.

2. MATERIALS AND METHODS

2.1 Ethics statement

This study was approved by the Ethics Committee of the Clinical Hospital Dubrava, Zagreb, Croatia (May 24, 2016).

2.2 Samples of human liver tissue and phase-contrast image acquisition

Twenty six phase-contrast images were recorded from unstained frozen sections belonging to eight patients diagnosed with the metastatic colon cancer in a liver. After recording, images were annotated according to procedure described in Section 2.3. All images were acquired in the phase-contrast mode on the light microscope Olympus BX51 with a DP50 camera, Japan, with magnifications 200x and 400x (eyepiece 10x and objective 20x and 40x). To confirm diagnosis, disease or tissues specific antigenes were immunohistochemically detected on paraffin-embedded liver sections by primary antibodies (Hepatocyte clone OCH1E5, CDX2 clone DAK-CDX2 and CK20 clone Ks20.8, all from Dako, Denmark) and visualized by labeled polymer (Dako Envision System, Denmark).

2.3 Ground truth generation

It is known that clinical annotation of histopathology data is a bottleneck in design and evaluation of histopathology image analysis related CAD algorithms [4], [9], [8]. Well annotated data are critical for optimization and performance evaluation of any learning-from-data approach, and especially for supervised classification systems [9]. Thus, generation of ground truth data has to be supervised by expert pathologists. This process, however, is highly time consuming for pathologists. Therefore, annotations are rarely pixel level precise and tend to contain numerous false positives and negatives [9]. Hence, to reduce burden on pathologists and to, possibly, reduce number of false positive and negatives we combined computational image segmentation method with pathologists' selection of cancer-related segment. Afterwards, selected cancer-related segment was refined according to pathologists' suggestions. In particular, a 3D acquired RGB image tensor $\underline{\mathbf{X}} \in \mathbb{R}_{0+}^{I_1 \times I_2 \times 3}$ was flattened into a matrix $\mathbf{X} \in \mathbb{R}^{3 \times I_1 I_2}$, where I_1 and I_2 stand, respectively, for number of rows and number of columns of the image. Segmentation is executed by means of nonnegative matrix factorization (NMF) algorithm with the ℓ_0 quasi-norm constraint imposed on latent variables (the image segments) [18]:

$$\begin{aligned} &\left(\hat{\mathbf{A}}, \hat{\mathbf{S}}\right) = \arg\min_{\mathbf{A},\mathbf{S}} \left\|\mathbf{X} - \mathbf{A}\mathbf{S}\right\|_2^2 \\ &s.t.\ \mathbf{A} \geq \mathbf{0}, \mathbf{S} \geq \mathbf{0},\ \left\|\mathbf{s}_j\right\|_0 \leq L \quad \forall j = 1,...,J. \end{aligned} \tag{1}$$

where $J=I_1 I_2$. $\mathbf{A} \in \mathbb{R}_{0+}^{3 \times M}$ and $\mathbf{S} \in \mathbb{R}_{0+}^{M \times J}$ respectively stand for basis (a.k.a. mixing) matrix and matrix of image segments. $\hat{\mathbf{A}}$ and $\hat{\mathbf{S}}$ stand respectively for estimates of $\mathbf{A}$ and $\mathbf{S}$. $\left\{\left\|\mathbf{s}_j\right\|_0\right\}_{j=1}^{J}$ stand for ℓ_0 quasi-norm (it counts number of nonzero entries of the vector $\mathbf{s}_j$) of the column vectors of $\mathbf{S}$. M is intrinsic dimension of $\mathbf{X}$ that in our application corresponds with the number of tissues present in the histopathological sample. In the study considered herein it was assumed M=6. L stands for the maximal number of tissues that can be simultaneously present at any pixel location. The acquired images were comprised of I_1=1037×I_2=1388 pixels with the size of the pixel footprint of 0.1098 μm^2. Since spatial resolution of the microscope was 0.45 μm it was justified to assume that only

one tissue structure occupies each pixel, [19]. Thus, we set L=1 in (1), which in combination with the nonnegativity represents constraints on **A** and **S** that ensure virtually essentially unique factorization of **X**. Columns of $\hat{\mathbf{A}}$ stand for spectra of tissue components in RGB color space, while rows of $\hat{\mathbf{S}}$, $\left\{\hat{\mathbf{s}}_m \in \mathbb{R}_{0+}^{1\times J}\right\}_{m=1}^{M}$, stand for spatial distributions of corresponding tissue structures. After unfolding, each segment $\left\{\hat{\mathbf{S}}_m \in \mathbb{R}_{0+}^{I_1\times I_2}\right\}_{m=1}^{M}$ was visualized and inspected by two pathologists (G. A. and A. P.). One segment, let us say $\hat{\mathbf{S}}_m^*$, was identified as cancer related and further post-processed in accordance with the pathologists' suggestions.

2.4 Structured AutoEncoder for deep subspace clustering and cancer diagnosis

Let us assume we have at disposal the prior knowledge on cancer reference (target) spectra in given representation domain (it can be the RGB image itself). Then, segmentation of the image in representation domain in combination with the prior information can be used for cancer diagnosis. That is, segment with the centroid closest to the target spectra (in term of some proximity measure) is labeled as cancerous. Thus, segmentation quality has direct influence on diagnostic performance. As opposed to single subspace-based methods such as principal component analysis or NMF, subspace clustering aims at seeking collection of low-dimensional implicit linear subspaces to fit given unlabeled data set and segment it into clusters according to subspaces they are generated from [20], [21], [22]. These methods represent data set using the self-representation model **X**=**XC**, where **C** stands for the representation matrix that needs to be learned from **X**. Clustering is performed by grouping eigenvectors of $\mathbf{L}=\mathbf{D}^{-1/2}\mathbf{A}\mathbf{D}^{1/2}$. Here, **L** stands for graph Laplacian and **D** is diagonal matrix with the entry $\mathbf{D}_{ii}=\sum_j \mathbf{A}_{ij}$. Affinity matrix is given as $\mathbf{A}=|\mathbf{C}|+|\mathbf{C}|^T$. Hence, performance of subspace clustering methods critically depends on **C**. Applying k-means algorithm to group top eigenvectors of **L** is known as spectral clustering [23], with computational complexity that is cubic in number of data points (pixels in the case of histopathological image). Another limitation of the existing subspace clustering methods is that they assume linear representation model even though data can lie on nonlinear manifold. Methods in [24] and [25] address this issue by formulating kernel-based subspace clustering for, respectively, single- and multi-view data. It is, however, unclear how to choose the kernel function. In addition to that, the out-of-sample problem is also the open issue of both linear and nonlinear kernel-based subspace clustering methods. That in combination with the cubic computational complexity, related to calculation of the eigenvectors of **L**, makes the existing subspace clustering methods infeasible for clustering large scale data sets such as images of histopathological specimens. To overcome issues addressed above, [16] proposed DL approach to subspace clustering in term of SAE. Assuming the neural network is comprised of N+1 layer, SAE in comparison with standard AE architecture imposes self-representation constraint on the hidden layer: $\mathbf{H}^{(N/2)}=\mathbf{H}^{(N/2)}\mathbf{C}$. Here, **C** is representation matrix learned from the input layer, i.e. data $\mathbf{H}^{(0)}=\mathbf{X}=\mathbf{XC}$ using some of the existing subspace clustering methods [20], [21], [22]. That preserves globality in learning $\mathbf{H}^{(N/2)}$. Locality is preserved by enforcing SAE to reconstruct the input **X** at the output layer $\mathbf{H}^{(N)}$. Section 3.1 presents more details of SAE architecture used for cancer diagnosis using phase-contrast images of unstained sections. To the best of our knowledge,

this is the first application of the SAE deep subspace clustering to intraoperative diagnoses of cancer from images of histopathological specimens.

2.5 U-net for segmentation and pixel-wise diagnosis

Fully convolutional neural networks (FCNs) [26] differ from CNNs in the fact that FCNs replace the fully connected layer with upsampling and deconvolution layer [26], [15]. Both of these layers are learnable and are considered as a backwards version of, respectively, pooling layer and convolutional layer. That yields characteristic U-shape of the network. FCNs are adopted for image segmentation due to two main reasons: (*i*) they can be applied to images of virtually any sizes, and (*ii*) they are capable for pixel-wise classification. Even though CNNs and/or FCNs require large number of training data to avoid overfitting, the problem can be alleviated up to some extent by using either transfer learning which yielded state-of-the-art performance on several histopathological datasets [27], or by slight modification of the original U-net architecture [26] such that it works with very few training images [28]. In this paper, we applied U-net in transfer learning mode for diagnosis of metastasis of colon cancer in a liver using phase-contrast images of unstained frozen sections. Results in Section 3.2 suggest that the U-net could reach competitive performance if large enough number of labeled images is available.

2.6 Spectral angle mapper diagnosis

We also used target detection algorithm from hyperspectral remote sensing: the SAM [29]. SAM is supervised pixel-based classifier that compares target cancer spectra $\mathbf{t} \in \mathbb{R}_{0+}^{3\times 1}$ with the pixel spectra $\mathbf{x}_j$ by calculating the angle $\alpha_j\left(\mathbf{x}_j, \mathbf{t}\right)$ between the two spectra. In our case **t** represents cancer spectra obtained as an average of all cancerous pixels on training images. Diagnosis is established through comparison of α_j with a threshold α^*:

$$D\left(\mathbf{x}_j\right) = \begin{cases} \text{cancer} & \textit{if} \quad \alpha_j \le \alpha^* \\ \text{non-cancer} & \textit{if} \quad \alpha_j > \alpha^* \end{cases} \tag{2}$$

Threshold α^* was estimated on the bases of eighteen images from the training set and the corresponding ground truth maps. It represents the arithmetic mean between average angle between the cancerous spectra and the target **t** and average angle between the non-cancerous spectra and the target **t**.

3. EXPERIMENTS AND RESULTS

3.1 Training and testing process

To obtain trustworthy results of intraoperative diagnosis we strictly separated training from testing data as recommended in [4]. The number of phase-contrast images of unstained sections per patient was either two (three patients) or four (five patients). Variation of number of images per patients was caused by the quality of tissue samples and frozen sections. See Section 4 for the more detailed discussion. Diagnostic models were trained and validated on eighteen annotated images (~70% of the overall number) belonging to five patients (~70% of the overall number) and tested on eight annotated images (~30% of the overall number) belonging to three patients (~30% of the overall number). We used SAE with vectorized 3×3 patches centered at each pixel of the phase-contrast images. The SAE applied to vectorized patches of the phase-contrast images contained three inner layers according to the architecture: 27×21×19×21×27. The `tanh` was used as nonlinear activation function. The k-means algorithm was applied to the self-referenced middle layer to obtain the final segmentation. Thereby, the k-means was cross-validated with the number of segments as hyper parameter. The best results were obtained for three segments. The segment with the centroid closest, in term of the angular proximity measure, to the target cancer spectra **t** was labeled as cancerous. Regarding the U-net applied on phase-contrast images, the encoder part of the network, the VGG-16 net, was kept on values pre-trained on the ImageNet database, while the decoder part of the network was trained and validated on ~70% of the annotated images (and patients), and tested on remaining ~30% of the images (and patients). Training and validation were performed only on the patches of the size 32×32 pixels that contained at least 20% of cancerous pixels. The U-net and the SAE diagnostic models were implemented in Tensorflow [30] and Keras [31] on QUADRO P6000 GPU card. The SAM diagnostic model was implemented in Matlab 2014b on a personal computer running under Windows 64-bit operating system with 64 GB of RAM using an Intel Core i7-3930K processor operating with a clock speed of 3.2 GHz. While training of the U-net and the SAE diagnostic models takes hours, diagnostic time is within one minute of the CPU time.

3.2 Performance scores

To quantify diagnoses performance we compared on eight test images labels predicted by the three diagnostic models (U-net, SAE and SAM) with the ground truths. As performance measures we used sensitivity, specificity, balanced accuracy and Dice coefficient (a.k.a. F_1 score). The worst value of all metrics corresponds to 0 and the best to 1. While sensitivity and specificity emphasize respectively errors in diagnoses of cancer and non-cancer pixels, balanced accuracy and Dice coefficient emphasize errors in diagnoses of both cancer and non-cancer pixels. Obtained results are shown in Table 1. Low value of the Dice coefficient implies that many predicted labels are false positive. That is visible in Fig. 1. It shows diagnostic maps (predicted labels) for the three methods, together with phase-contrast images and ground truth maps. Given the fact that very few researches have analyzed frozen sections so far [8] and given the fact that, to the best of our knowledge, no

research results for CAD based on phase-contrast images of unstained frozen section were published so far, we consider achieved performance as promising. In particular, very recently research [12] provided intraoperative computer aided assessment of squamous cell carcinoma on tongue using hyperspectral images of H&E stained frozen sections. Experiments on seven *ex vivo* tongue-tumor specimens yielded sensitivity=0.94 and specificity=0.68. Hence sensitvity=0.945 and specificity=0.729 achieved by the U-net on phase-contrast images of unstained frozen sections is promising result. Further performance improvement is expected after optimizing hyper-parameters such as the input patch size and nonlinear activation functions.

Table 1. Diagnostic performance (mean ± standard deviation) achieved by the U-net, SAE and SAM models on eight phase-contrast images of unstained frozen sections. Sections were collected from the three patients diagnosed with the metastasis of colon cancer in a liver.

	Balanced accuracy	**Sensitivity**	**Specificity**	**Dice coefficient**
U-net	0.837±0.080	0.945±0.080	0.729±0.080	0.452±0.254
SAE	0.700±0.170	0.827±0.310	0.574±0.056	0.346±0.211
SAM	0.517±0.025	0.511±0.172	0.524±0.150	0.197±0.120

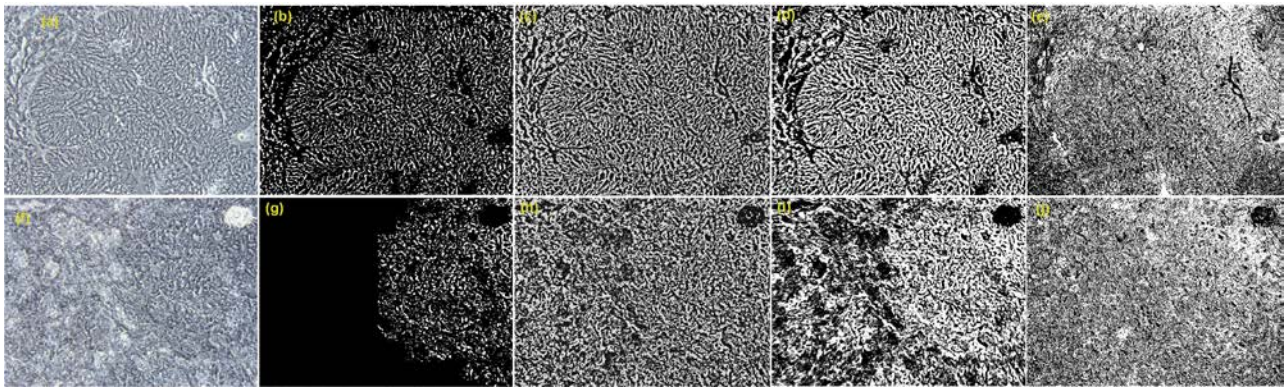

Figure 1. (a) and (f) RGB phase-contrast images; (b) and (g) ground truths; (c) and (h) labels predicted by the U-net; (d) and (i) labels predicted by the SAE; (e) and (j) labels predicted by the SAM.

4. DISCUSSION

There are multiple factors that affect reproducibility of the quality of frozen sections. They include tissue type that affects the freezing time; treatment and procedures during surgery, such as: drugs, time from excision till freezing in laboratory; thickness of the specimen; melting of the specimen under the microscope; drops of water on the surface of the specimen and frozen crystals in the specimen; as well as skill of the laboratory technician. All these factors contribute to variations in frozen sections preparation and affect diagnostic performance reported in Section 3. In this regards, Fig. 2 illustrates how mentioned factors contribute to the variation of the phase-contrast images of

the unstained frozen sections. Thus, we had to pay special attention during sample collection process to the quality of acquired images and discard phase-contrast images such as the one shown in Fig. 2b.

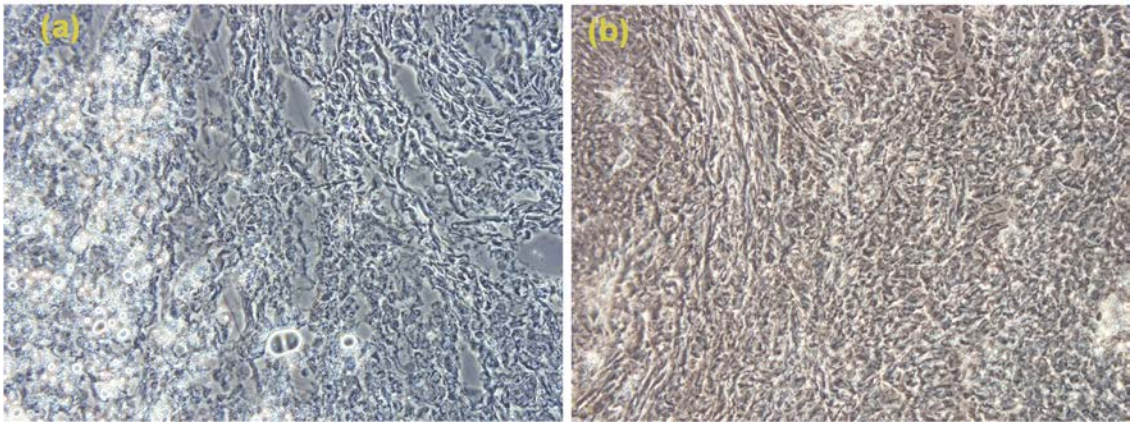

Figure 2. Examples of the phase contrast images of unstained frozen sections. (a) Good quality. Tumor is in gray-blue color. (b) Poor quality.

5. CONCLUSIONS

This paper presents three methods for intraoperative computer aided diagnosis of metastatic colon cancer in a liver from phase-contrast images of unstained frozen sections. The methods are aimed to assist pathologist, as a second reader, during intraoperative diagnosis. To the best of our knowledge this is the first work attempting to discriminate metastatic colon cancer cells in liver from non-cancerous cells in intraoperative diagnosis using images of unstained frozen sections. In particular, two deep learning methods, the U-net and the SAE-based deep subspace clustering, were trained for diagnosis. The U-net has potential to reach competitive diagnostic performance provided that: more labeled images are available; variation of the quality of phase-contrast images, cause by variations in frozen section collection and preparation process, is reduced. In addition to that, further improvement in diagnostic performance of proposed methods is possible through the increase of the accuracy of ground truth. Quality of generated ground truth is in our approach possibly affected by image segmentation method. That is, pathologists identified one segment as cancer related and focused on its refinement. In the future work it is planned that, through software assistance, pathologists label cancerous pixels directly.

ACKNOWLEDGEMENTS

This work was supported through grant IP-2016-06-5235 "Structured Decompositions of Empirical Data for Computationally-Assisted Diagnosis of Disease" funded by the Croatian Science Foundation; European Regional Development Fund under the grant KK.01.1.1.01.0009 (DATACROSS); bilateral Chinese-Croatian project "Structure constrained decompositions for enhancement and segmentation of PET/CT and OCT images" funded by Ministry of Science,

Education and Sports Republic of Croatia. We gratefully acknowledge the support of NVIDIA Corporation with the donation of the QUADRO P6000 GPU used for this research.

REFERENCES

[1] Stewart, B. W., Wild, C. P., Eds., World Cancer Report 2014. Lyon: IARC, 2014. [Online]. Available: /publications.iarc.fr/Non-Series-Publications/World-Cancer-Reports/World-Cancer-Report-2014

[2] Steknvist, B., Westaman-Naeser, S., Holmquist, J., Nordin, B., Veqellius, J., Eriksson, O., Fox, C. H., "Computerized nuclear morphometry as an objective method for characterizing human cancer cell populations," Cancer Res. 38, 4688-4697 (1978).

[3] Rubin, R., Strayer, D., Rubin, E., McDonald, J., Eds., [Rubin's Pathology Clinicopathologic Foundations of Medicine], 6th ed., Philadelphia, PA, USA: Williams & Wilkins (2012).

[4] Gurcan, M. N., Boucheron, L. E., Can, A., Madabhushi, A., Rajpoot, N. M., and Yener, B, "Histopathological Image Analysis: A Review," IEEE Rev. Biomed. Eng. 2, 147-171 (2009).

[5] Litjens, G., Sanchez, C. I., Timofeeva,N., Hermsen, M., Nagtegaal, I., Kovacs, I., Hulsbergen van de Kaa, C., Bult, P., van Ginneken, B., and van der Laak, J., "Deep learning as a tool for increased accuracy and efficiency of histopathological diagnosis," Scientific Reports 6, article no. 26286 (2016).

[6] Spanhol, F. A., Oliveira, L. S., Petitjean, C., and Heutte, L., "A Dataset for Breast Cancer Histopathological Image Classification," IEEE Trans. Biomed. Eng. 63, 1455-1462 (2016).

[7] Xing, F., Xie, Y., Su, H., Liu, F., and Yang, L., "Deep Learning in Microscopy Image Analysis: A Survey," IEEE Trans. Neural Net. Learn. Syst. 29, 4550-4568 (2018).

[8] Komura, D., and Ishikawa, S., "Machine Learning Methods fir Histopathological Image Analysis," Comp. and Struct. Biotech. J. 16, 34-42 (2018).

[9] Janowczyk, A., and Madabhushi, A., "Deep learning for digital pathology image analysis: A comprehensive tutorial with selected cases," J. Path. Inform., 7-29 (2016).

[10] Kothari, S., Phan, J. H., Stokes, T. H., Osunkoya, A. O., Young, A. N., and Wand, M. D., "Removing batch effects from histopathological images for enhanced cancer diagnosis," IEEE J. Biomed. Health Inf. 18, 765-772 (2014).

[11] Abas, F. S., Gokozan, H. N., Goksel, B., Otero, J. J., and Gurcan, M. N., "Intraoperative neuropathology of glioma recurrence: cell detection and classification," in Proc. SPIE 9791, Med. Imag. 2016 - Digital Pathology, vol. 9791, 2016, art. no. 979109.

[12] Manni, F., van der Sommen, F., Zinger, S., Kho, E., Brouwer de Koning, S., Ruers, T., Shan, C., Schleipen, J., and de With, P. H. N., "Automated tumor assessment of squamous cell carcinoma on tongue cancer patients with hyperspectral imaging," in Proc. SPIE 10951, Med. Imag. 2019 - Image-Guided Proc., Robotics Interventions and Modeling, vol. 10951, 2019, article no. 109512K.

[13] Xu, X., Wu, Q., Wang, S., Liu, J., Sun, J., and Cichocki, A., "Whole Brain fMRI Pattern Analysis Based on Tensor Neural Network," IEEE Access 6, 29297-29305 (2018).

[14] Qiu, J. X., Yoon, H. J., Feran, P. A., and Tourassi, G. T., "Deep Learning for Automated Extraction of Primary Sites From Cancer Pathology Reports," IEEE J. Biomed. Health Inf. 22, 244-251 (2018).

[15] Hu, Z., Tang, J., Wang, Z., Zhang, K., Zhang, L., and Sun, Q., "Deep Learning for Image-based Cancer Detection and Diagnosis - A Survey," Pattern Recognition 83, 134-149 (2018).

[16] Peng, X., Feng, J., Xiao, S., Yau, W. Y., Zhou, J. T., and Yang, S., "Structured AutoEncoders for Subspace Clustering," IEEE Trans. Image Proc. 27, 5076-5086 (2018).

[17] Ronneberger, O., Fischer, P., and Brox, T., "U-net: Convolutinal networks for biomedical image segmentation," in Proc. 18th Int. Conf. Med. Image Comput.-Assist. Intervent., vol. 9351, 2015, pp. 234-241.

[18] Peharz, R., and Pernkopf, F., "Sparse nonnegative matrix factorization with ℓ^0-constraints," Neurocomputing 80, 38-46 (2012).

[19] Kopriva, I., Popović Hadžija, M., Hadžija, M., and Aralica, G., " Unsupervised segmentation of low-contrast multichannel images: discrimination of tissue components in microscopic image of unstained specimen," Scientific Reports 5, article no. 11576 (2015).
[20] Elhamifar E., and Vidal, R., “Sparse subspace clustering: Algorithm, theory, and applications,” IEEE Trans. Pattern Anal. Mach. Intell. 35, 2765–2781 (2013).
[21] Liu, G., Lin, Z., Yan, S., Sun, J., Yu, Y., and Ma, Y., “Robust recovery of subspace structures by low-rank representation,” IEEE Trans. Pattern Anal. Mach. Intell. 35, 171–184 (2013).
[22] Brbić, M., and Kopriva, I., "ℓ_0 Motivated Low-Rank Sparse Subspace Clustering," IEEE Trans. Cybernet., doi: 10.1109/TCYB.2018.2883566.
[23] von Luxburg, U., "A tutorial on spectral clustering," Stat. Comput. 17, 395–416 (2007).
[24] Xiao, S., Tan, M., Xu, D., and Dong, Z. Y., "Robust kernel low-rank representation," IEEE Trans. Neural. Netw. Learn. Syst. 27, 2849-2853 (2016).
[25] Brbić, M., and Kopriva, I., "Multi-view Low-rank Sparse Subspace Clustering," Patt. Recog. 73, 247-268 (2018).
[26] Long, J., Shelhamer, E., and Darell, T., "Fully convolutional networks for semantic segmentation," in Proc. IEEE Conf. Comput. Vis. Pattern Recognit., 2015, pp. 3431-3440.
[27] Janowczyk, A., Basavanhally, A., and Madabhushi, A., “Stain Normalization using Sparse AutoEncoders (StaNoSA): Application to digital pathology,” Comput. Med. Imag. Graph. 57, 50–61 (2017).
[28] Madabhushi A., and Lee, G., “Image analysis and machine learning in digital pathology: Challenges and opportunities,” Med. Image Anal. 33, 170–175 (2016).
[29] Chang, Ch. -I., Ed., [Hyperspectral Data Exploitation - Theory and Applications], Wiley-Interscience (2007).
[30] TensorFlow White Papers. [online] at: https://www.tensorflow.org/about/bib [Last accessed on July 10 2019].
[31] Keras FAQ: Frequently Asked Kears Questions. [online] at: https://keras.io/getting-started/faq/#how-should-i-cite-keras [Last accessed on July 10 2019].